

Research Article

Dynamic Aerothermal Analysis of a Cone-Cylinder Flight Body

Jun Zhang , Guangchen Jia, Sibanda Gibson Mkumbuzi, and Yu Wu

College of Engineering Science and Technology, Shanghai Ocean University, Shanghai 201306, China

Correspondence should be addressed to Jun Zhang; zhangjun@shou.edu.cn

Received 29 January 2020; Revised 30 June 2020; Accepted 4 July 2020; Published 21 July 2020

Academic Editor: Feng Qu

Copyright © 2020 Jun Zhang et al. This is an open access article distributed under the Creative Commons Attribution License, which permits unrestricted use, distribution, and reproduction in any medium, provided the original work is properly cited.

Exploring the aerothermal characteristic of a flight body has great military applications in tracking, locating, thermal protection, and infrared stealth technologies. Available studies are mostly focused on the transient aerothermal characteristics of vehicles in some specific flight datum, which are not able to satisfy the requirements in real-time tracking for an infrared system. This paper probes into a method of dynamic thermal analysis of a cone-cylinder flight body with a high spinning speed. Firstly, a theoretical model for analyzing the dynamic aerothermal characteristics is established using the thermal node-network method. Then, trajectory datum and the convective heat-transfer coefficients are solved simultaneously. Besides, the trajectory datum in supersonic, transonic, and subsonic regimes is separately defined as the boundary conditions, and fluid-thermal analysis methods are implemented by a combination of sliding mesh and multicoordinate approaches. Finally, the flow characteristics are analyzed and compared with disregarding the rotational speed. The results demonstrate that there are significant differences between the two cases, especially at the high-speed regimes. This study further confirms that it is essential to conduct the aerothermal analysis from a dynamic point of view, and taking the impacts of coupling motion into account is also of vital importance.

1. Introduction

For flight vehicles, aerothermal responses are crucial in the testing of flight parameters for an infrared radiation tracking measurement system, such as coordinate, attitude, and yaw [1–4]. Furthermore, aerothermal analysis methods are also essential to design the thermal protection structure and infrared stealth technology [5–9]. However, it is hard to accurately assess the aeroheating characteristics due to physical uncertainties and time-varying properties. In the past few decades, a series of numerical methods to estimate the aerothermal characteristics for hypersonic vehicles were proposed [10–16]. Knight et al. [17–19] appraised the capability for CFD simulation of hypersonic shock wave laminar boundary layer interaction for a double wedge model and compared with experimental heat transfer and schlieren visualization. Zheng and Qiu [20] performed the uncertainties in aerodynamic force and heating characteristics of the wing of a hypersonic vehicle accounting for uncertain-but-bounded geometric parameters. Ahmed and Qin [21–25] explored extensive research on a spiked blunt body. They investigated the air-

flow over the conical, disk, and flat spiked bodies and analyzed the flow asymmetry around axisymmetric spiked blunt bodies at hypersonic regimes. Qin et al. [26] conducted a loosely coupled fluid-thermal method to explore the aerodynamic thermal responses of a spiked blunt in a hypersonic regime and relevant flow variation.

Unfortunately, researchers have mainly focused on the transient aerodynamic heating of vehicle in some specific flight states [27–29]. However, aeroheating characteristics on the surface of vehicles are not only determined by the current flight state but also related closely to the heat transfer environment during the flight, which is a progressive, lasting, and dynamic process [30]. Therefore, the results of the transient thermal analysis were inevitably deviated from a practical situation, which cannot be used for real-time tracking and monitoring of the IR detecting system [31]. For example, Duda [32] formulated an effective method which can be employed to calculate the transient heat fluxes, and the algorithms were used to assess the transient temperature distribution in a whole component based on measured temperatures in selected points on the component surface.

Research on the real-time infrared radiation imaging simulation method of aircraft skin with aerodynamic heating effect, Li et al. [33] employed a dynamic simulation method to carry out the research of infrared radiation (IR) characteristics of an aircraft during the flight, and the aeroheating model and environmental radiation model were established for solving the heat balance equations.

Additionally, high-speed spinning is the major mode to maintain flying stability for some vehicles, but related to the aeroheating characteristics for a flight body with coupling motion of precession, spinning, and pitching is limited. Particularly, the effects of spinning are often neglected. For example, Siltan [34] adopted the CFD method to analyze the flow behaviors for a flying projectile under different velocities and attack angles, but the rotational speed was ignored. Although the simulated values of drag and lift coefficients were basically consistent with the calculated data of semiempirical formulas and experiments, there was a remarkable deviation between the Magnus force and moment with the experimental results. On the contrary, James [35] investigated the flow characteristics of airflow around the M910 projectile under different rotating speeds. The simulated results acquired by employing the RANS/LES mixed turbulence model were in good accordance with the experimental values in subsonic and transonic conditions.

Therefore, the dynamic aerothermal characteristics of the flight body in coupled motions of precession, spinning, and pitching are necessary studies. In this article, dynamic aerothermal related to the surface of a cone-cylinder spinning flight body is reconstructed using updated modeling approaches. Firstly, the six degrees of freedom (6-DOF) trajectory model is established, and the motion characteristics are analyzed at different launch conditions. Then, the trajectory datum and the convective heat-transfer coefficients are simultaneously solved by the Runge-Kutta method, and the influencing factors are also analyzed.

2. 6-DOF Trajectory Model

A kind of spinning projectile is taken as the research object to investigate the continuous aeroheating characteristics on the surface of a flight body in the coupled motions of precession, spinning, and pitching. The simplified structural model is depicted in Figure 1; the lengths of the conical section and the cylindrical section are, respectively, indicated by L_1 and L_2 . The diameter of the cylindrical section is d .

The 6-DOF kinetic model is established by the exterior ballistic theory to describe the movement regularities of the cone-cylinder spinning flight body. The modeling procedures are listed below: Firstly, the reference coordinate systems are created, including the ground coordinate, datum coordinate, ballistic coordinate, body coordinate, and body-axis coordinate systems. Then, the dynamic loads are analyzed, including the gravity, drag, lift, Magnus force, static moment, equatorial and polar damping moment, and Magnus moment.

Based on the general theoretical analysis above, the kinematic equations and the kinetic equations are derived

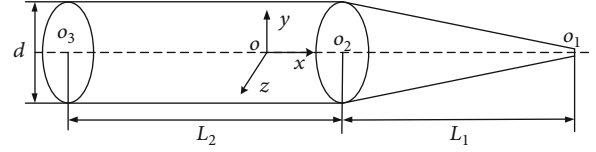


FIGURE 1: Geometric model.

according to the momentum theorem and mass center motion theorem in the ballistic coordinate system.

$$\begin{cases} m \frac{dv}{dt} = \sum \mathbf{F}_x, \\ mv \frac{d\psi_1}{dt} \cos \psi_2 = \sum \mathbf{F}_y, \\ mv \frac{d\psi_2}{dt} = \sum \mathbf{F}_z, \end{cases} \quad (1)$$

$$\begin{cases} \frac{dx}{dt} = v \cos \psi_1 \cos \psi_2, \\ \frac{dy}{dt} = v \sin \psi_1 \cos \psi_2, \\ \frac{dz}{dt} = v \sin \psi_2. \end{cases} \quad (2)$$

Similarly, the kinetic equations and kinematic equations are derived in accordance with the theorem of momentum moment in the body-axis coordinate system.

$$\begin{cases} \frac{d\omega_\xi}{dt} = \frac{1}{C} \sum \mathbf{M}_\xi, \\ \frac{d\omega_\eta}{dt} = \frac{1}{A} \sum \mathbf{M}_\eta - \frac{C}{A} \omega_\xi \omega_\zeta + \omega_\zeta^2 \tan \varphi_2 + \frac{A-C}{A} \beta_1 \phi'', \\ \frac{d\omega_\zeta}{dt} = \frac{1}{A} \sum \mathbf{M}_\zeta + \frac{C}{A} \omega_\xi \omega_\eta - \omega_\eta \omega_\zeta \tan \varphi_2 + \frac{A-C}{A} \beta_2 \phi'', \end{cases} \quad (3)$$

$$\begin{cases} \frac{d\varphi_1}{dt} = \frac{\omega_\zeta}{\cos \varphi_2}, \\ \frac{d\varphi_2}{dt} = -\omega_\eta, \\ \frac{d\phi}{dt} = \omega_\xi - \omega_\zeta \tan \varphi_2. \end{cases} \quad (4)$$

Accordingly, the 6-DOF trajectory model can be obtained by simultaneous equations (1), (2), (3), and (4) and constraint equations (5).

$$\begin{cases} \sin \delta_1 = \frac{\cos \varphi_2}{\cos \delta_2} \sin (\varphi_1 - \psi_1), \\ \sin \delta_2 = \cos \psi_2 \sin \varphi_2 - \sin \psi_2 \cos \varphi_2 \cos (\varphi_1 - \psi_1), \end{cases} \quad (5)$$

where x, y, z are the mass center coordinates; $\mathbf{F}_x, \mathbf{F}_y, \mathbf{F}_z$ are the force components in the ballistic coordinate system;

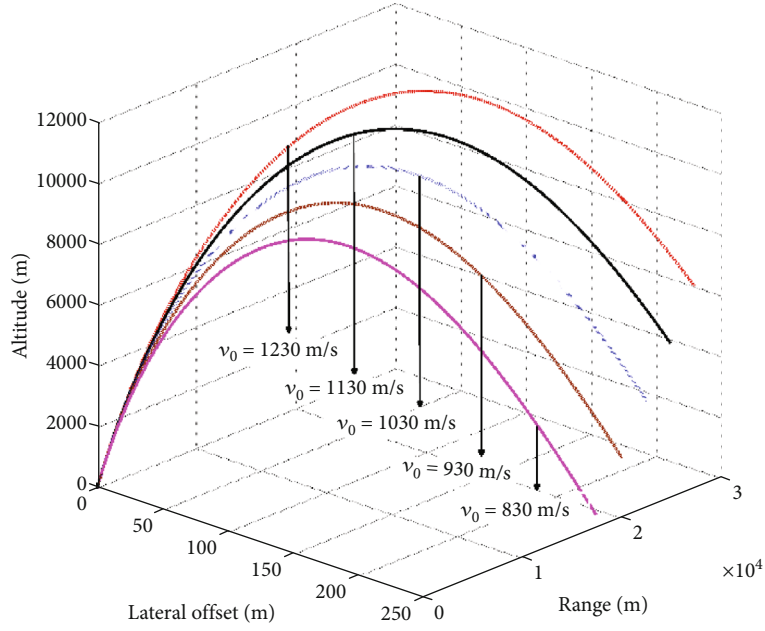


FIGURE 2: Trajectory curves at different initial velocities.

M_{ξ} , M_{η} , M_{ζ} are the moment components that of acting on the projectile in the body-axis coordinate system; ω_{ξ} , ω_{η} , ω_{ζ} are the components of angular speed.

3. Theoretical Model of Aerodynamic Heating

3.1. Surface Element Division. The domain decomposition and surface element division are essential to derive the theoretical model. In this paper, the node-network method is proposed to generate the surface elements and take the center of each element as a compute node. The cone-shaped angle α is equally separated into n parts, and the fan-shaped radius R is evenly divided into n_1 parts. Then, according to the rules of equal areas, the area of a surface panel Δs and R_i is, respectively, expressed as

$$R_i = \sqrt{\frac{iR^2}{n_1}}, \quad i = (1, n_1), \quad (6)$$

$$\Delta s = \frac{\pi d R}{2n n_1}. \quad (7)$$

The cylindrical surface is evenly divided into n_2 parts in an axial direction, and the division numbers are identical to the cone-shaped angle in a radial direction. For equalizing the area of the surface panel, n_2 yields

$$n_2 = \frac{2n_1 L_2}{\sqrt{L_1 + (d^2/4)}}. \quad (8)$$

In the body coordinate system, column coordinates of node (i, k) and normal vectors of the surface panel on the conical surface are expressed as

$$\begin{cases} r(i, k) = \frac{d}{2R} \times \sqrt{\frac{i-1}{2n_1} R^2 + \frac{i}{2n_1} R^2}, \\ \varphi(i, k) = \frac{2\pi}{n} k, \\ z(i, k) = -\frac{L_1}{R} \times \sqrt{\frac{i-1}{2n_1} R^2 + \frac{i}{2n_1} R^2} + L_1 + L_2, \end{cases} \quad (9)$$

$$\mathbf{n}_i = \left[\frac{L_1}{R} \cos\left(\frac{2\pi}{n} k\right), \frac{L_1}{R} \sin\left(\frac{2\pi}{n} k\right), \frac{d}{2R} \right]. \quad (10)$$

Similarly, the column coordinates of node (j, k) and normal vectors of the surface panel on the cylindrical surface are expressed as

$$\begin{cases} r(j, k) = \frac{d}{2}, \\ \varphi(j, k) = \frac{2\pi}{n} k, \\ z(j, k) = \frac{L_2}{n_2} (m_1 - j - 1) + \frac{L_2}{2n_2} + L_2, \end{cases} \quad (11)$$

$$\mathbf{n}_j = \left[\cos\left(\frac{2\pi}{n} k\right), \sin\left(\frac{2\pi}{n} k\right), 0 \right]. \quad (12)$$

3.2. Convective Heat Transfer Model. In this section, a theoretical model for solving the convective heat transfer coefficient on the surface of the flight body will be constructed from the theory of heat transmission. For taking the impacts of spinning speed into account, the absolute velocity in the rotating coordinate system is assumed to be the flight velocity; then, according to the velocity synthesis theorem,

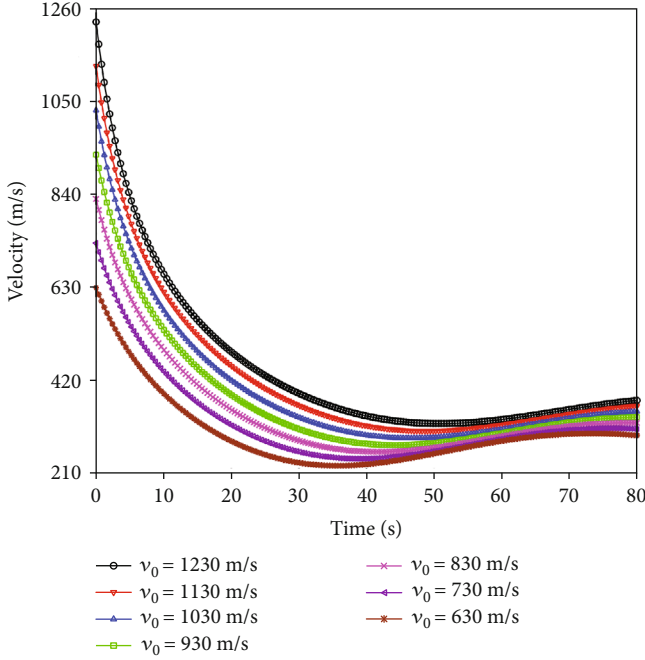


FIGURE 3: Velocity at different initial velocities.

$$\mathbf{u} = \mathbf{v} + \boldsymbol{\omega} \times \mathbf{r}, \quad (13)$$

where \mathbf{u} is the velocity vector in the rotating coordinate system, \mathbf{v} is the velocity vector in the inertial coordinate system, and $\boldsymbol{\omega}$ is the angular speed vector. The initial angular speed is defined as

$$\boldsymbol{\omega}_0 = \frac{2\pi\mathbf{v}_0}{\eta d}. \quad (14)$$

If the standard-sea-level atmospheric parameters are regarded as the airflow parameters of the projectile at the launch position, and the relations between temperature, density, and pressure of the freestream can be, respectively, expressed as

$$T_\infty = 288.15 - \frac{65}{10000}y, \quad (15)$$

$$\rho_\infty = 1.225 \left(\frac{T_\infty}{288.15} \right)^{4.2558}, \quad (16)$$

$$P_\infty = 101325 \left(\frac{T_\infty}{288.15} \right)^{5.2558}. \quad (17)$$

The adiabatic wall temperature T_0 and the recovery temperature T_r are formulated as

$$T_0 = T_\infty \left(1 + \frac{\kappa - 1}{2} Ma_\infty^2 \right), \quad (18)$$

$$T_r = T_\infty \left(1 + \gamma \frac{\kappa - 1}{2} Ma_\infty^2 \right), \quad (19)$$

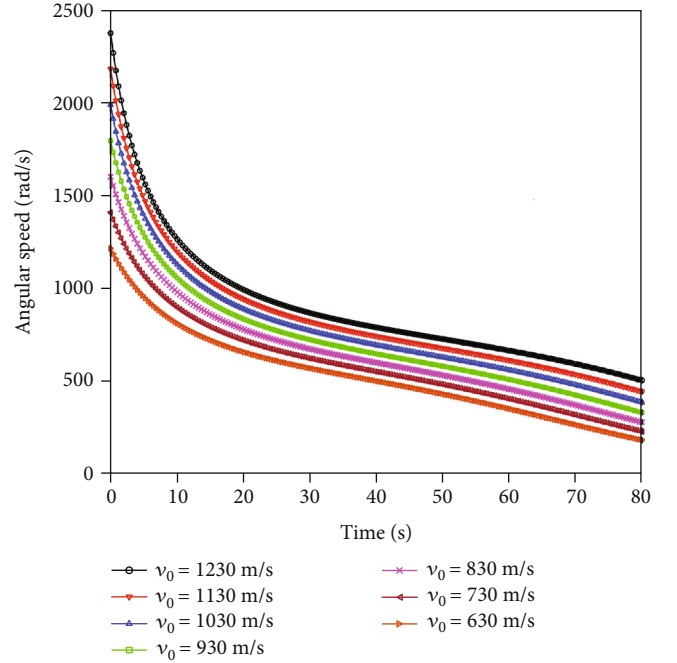


FIGURE 4: Angular speed at different initial velocities.

where y is the flight altitude and γ is the temperature recovery coefficient. When the flow is laminar, $\gamma = \sqrt{\overline{Pr}}$, otherwise, $\gamma = \sqrt[3]{\overline{Pr}}$.

According to the fluid mechanics and heat-transfer theories, the local Nusselt number can be approximately substituted for calculating the forced convection heat transfer on a flat plate, when the high-speed airflow is passing over the cylindrical surface longitudinally.

$$\begin{cases} \text{Nu}_{i,v}^* = 0.332 \times (\text{Re}_{i,v}^*)^{1/2} (\text{Pr}^*)^{1/3}, & \text{Re}_{i,v}^* \leq 5 \times 10^5, \\ \text{Nu}_{i,v}^* = 0.0296 \times (\text{Re}_{i,v}^*)^{4/5} (\text{Pr}^*)^{1/3}, & 5 \times 10^5 < \text{Re}_{i,v}^* \leq 10^7, \\ \text{Nu}_{i,v}^* = 0.185 \times (\text{Re}_{i,v}^*) (\lg \text{Re}_{i,v}^*)^{-2.584} (\text{Pr}^*)^{1/3}, & 10^7 < \text{Re}_{i,v}^* \leq 10^9, \end{cases} \quad (20)$$

where $\text{Nu}_{i,v}^*$, Pr^* , $\text{Re}_{i,v}^*$ are the local Nusselt number, Prandtl number: $\text{Pr}^* = \mu^* c_p^* / \lambda^*$, and Reynolds number: $\text{Re}_{i,v}^* = \rho^* u x / \mu^*$; x_i , λ^* , and μ^* are the distance from a compute node to the warhead, the thermal conductivity, and the viscosity coefficient.

$$\lambda^* = 2.72 \times 10^{-4} (T^*)^{4/5}, \quad (21)$$

$$\mu^* = 2.27 \times 10^{-8} \frac{(T^*)^{3/2}}{T^* + 198.6}. \quad (22)$$

It is known that the compressible flow theory cannot be used in predicating the aerodynamic heat flux using an implicit function with the given physical quantity. In order to solve the problem, a reference temperature method that calculates the boundary-layer parameters in the flow field is proposed. The transport and thermodynamic properties are

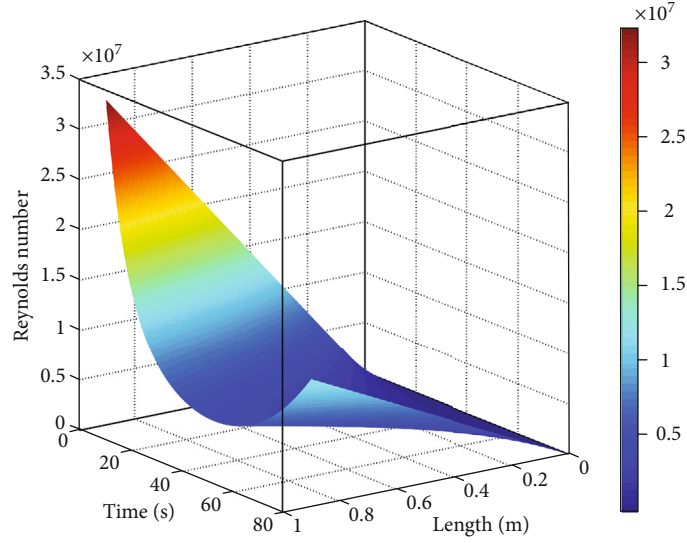


FIGURE 5: 3-D distribution of the Reynolds number.

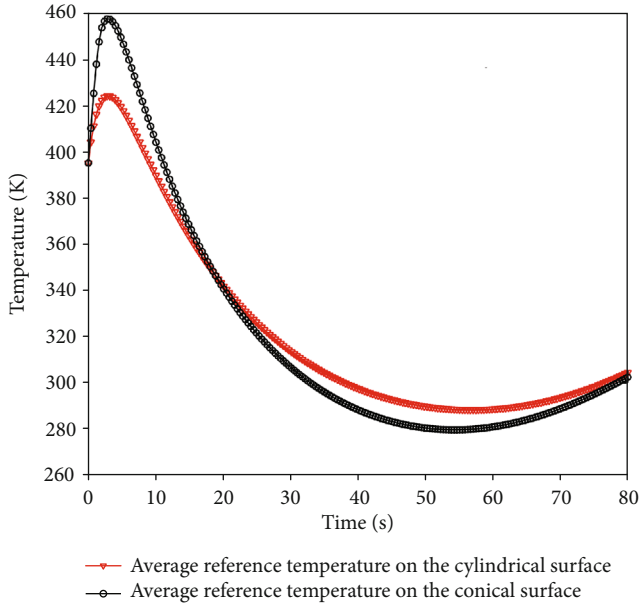


FIGURE 6: Average reference temperatures.

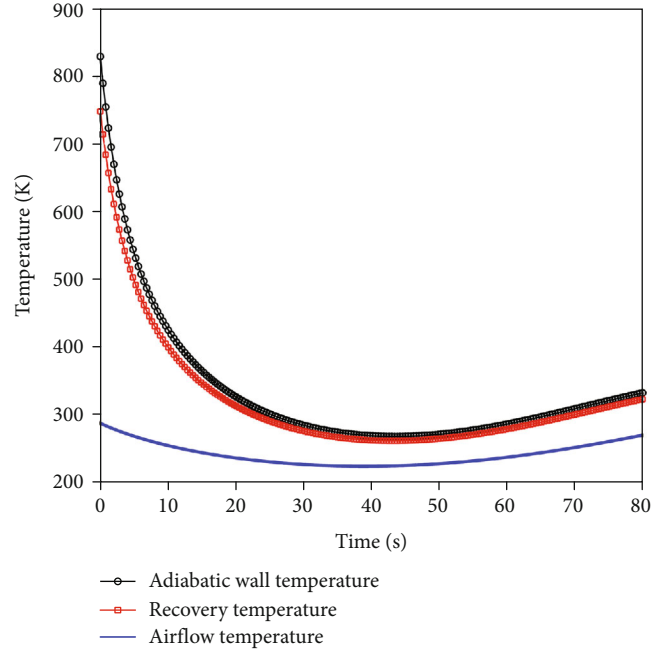


FIGURE 7: Adiabatic wall, recovery, and airflow temperature.

evaluated at the reference temperature (T^*) which indicates positions inside the boundary layer [22].

$$T^* = T_{\infty} + 0.5(T_w - T_{\infty}) + 0.22(T_f - T_{\infty}). \quad (23)$$

According to the theory of heat transmission, a relation between the local Nusselt number and the heat-transfer coefficient is defined as

$$Nu_{i,v}^* = \frac{h_i^* x_i}{\lambda^*}. \quad (24)$$

Then, the coefficient of convection heat transfer on the cylindrical surface can be expressed as

$$\begin{cases} h_{i,c}^* = 0.332x_i^{-1/2}(\mu^*c^*)^{1/3}(\lambda^*)^{2/3}\left(\frac{u\rho^*}{\mu^*}\right)^{1/2}, & Re_{i,v}^* \leq 5 \times 10^5, \\ h_{i,c}^* = 0.0296x_i^{-1/5}(\mu^*c^*)^{1/3}(\lambda^*)^{2/3}\left(\frac{u\rho^*}{\mu^*}\right)^{4/5}, & 5 \times 10^5 < Re_{i,v}^* \leq 10^7, \\ h_{i,c}^* = 0.185u\rho^*(\mu^*)^{-2/3}(c^*)^{1/3}(\lambda^*)^{2/3}\left(\lg \frac{u\rho^*x_i}{\mu^*}\right)^{-2.584}, & 10^7 < Re_{i,v}^* \leq 10^9. \end{cases} \quad (25)$$

The coefficient of convection heat transfer on the conical surface can be approximately calculated by the circle theorem of hydrodynamics [31].

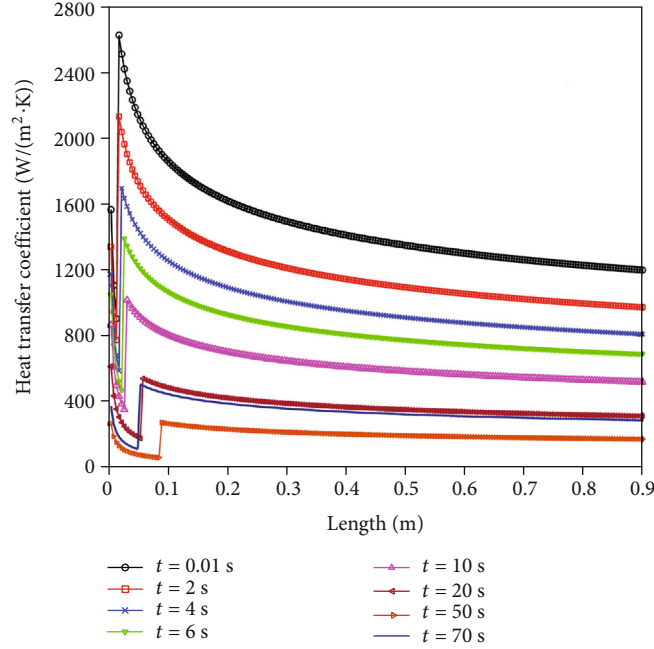


FIGURE 8: Transient heat transfer coefficients.

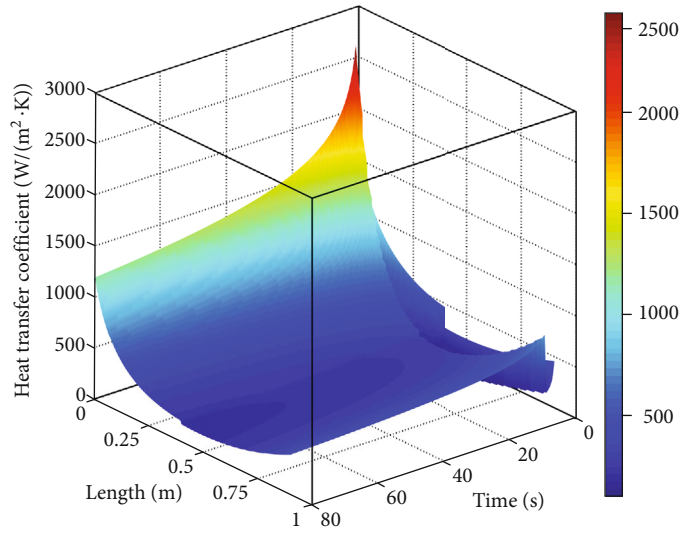


FIGURE 9: Convection heat transfer coefficient.

$$\begin{cases} h_{i,p}^* = 0.332\sqrt{3}x_i^{-1/2}(\mu^*c^*)c^{*1/3}(\lambda^*)^{2/3}\left(\frac{u\rho^*}{\mu^*}\right)^{1/2}, & \text{Re}_{i,v}^* \leq 5 \times 10^5, \\ h_{i,p}^* = 0.03481x_i^{-1/5}(\mu^*c^*)^{1/3}(\lambda^*)^{2/3}\left(\frac{u\rho^*}{\mu^*}\right)^{4/5}, & \text{Re}_{i,v}^* > 5 \times 10^5. \end{cases} \quad (26)$$

4. Theoretical Calculation and Discussion

4.1. Trajectory Calculation. The primary data for trajectory calculation is shown below: the lengths of conical and cylindrical sections are 400 mm and 500 mm. The cylindrical diameter is 155 mm, and the mass is 46.5 kg. The distance

from the center of mass to the warhead is 550 mm. The launch velocity, shot angle, and flight time are 1030 m/s, 45°, and 80 s, respectively. The equatorial moment of inertia is 1.814 kg·m², and the pole moment of inertia is 0.163 kg·m². The Runge-Kutta method is adopted to simultaneously solve the 6-DOF trajectory model and the aerodynamic heat transfer model, and the ballistic parameters and the heat-transfer coefficients with flight time can be obtained synchronously. Figure 2 presents the trajectory curves at different launch velocities, where the x , y , and z , respectively, indicate the range, flight altitude, and lateral offset. The lateral offset is caused by the gyroscopic orientation effects and gravitational deflection in the trajectory tangent.

Figures 3 and 4, respectively, show the flight velocity and spinning speed at different initial velocities. It is shown that the velocity conforms to decrease exponentially in ascending order. Yet at the parabola apexes, there is not the minimum before the air resistance acceleration is greater than the component of the gravity acceleration in the vertical direction. Moreover, the velocity approaches the minimum when the center of mass acceleration is zero, and then, it starts to rise reversely in the terminal trajectory. Thru comparison, it can be found that the velocity in the ascending period is greater than that in the descending at the same flight altitude. Besides, the faster the initial velocity is, the quicker the attenuation rates will be, and the attenuation rate of angular speed in the ascending period is faster than in the descending. It is known that the ratio of flight velocity and rotational speed approaches the minimum in the launch position, and the peak appears at the parabola apexes, yet the ratio starts to drop as the velocity is increasing in the terminal trajectory.

4.2. Dynamic Heat-Transfer Coefficients. Figure 5 presents the 3-D distribution of the Reynolds number. As shown in Figure 6, the average reference temperatures on the cylindrical surface and conical surface can be obtained.

From the results, each compute node corresponds to a Reynolds number and a reference temperature, and the maximum Re is about 3.3×10^7 , which covers the calculation range from laminar to turbulence flow. In the first 20 seconds of the trajectory, the average reference temperature of the conical part is significantly higher than that of the cylindrical part, especially in a short time after launching, but the temperature attenuation is also faster. After 20 seconds, the average reference temperature of the conical part is lower than that of the cylindrical part.

Figure 7 presents the adiabatic wall temperature, recovery temperature, and airflow temperature. As shown in Figure 8, the transient heat transfer coefficients on the surface of the flight body can be obtained. From the results, the trends of adiabatic wall temperature and recovery temperature are basically consistent with the flight velocities, but the change extents are relatively different. The differences between adiabatic wall temperature and recovery temperature are mainly reflected in the first 20 seconds of the trajectory. The airflow temperature is first to decrease and then increase with the change in flight altitude.

Figure 9 presents the 3-D distribution of the convection heat transfer coefficient on the surface of the flight body. The results demonstrate that the heat-transfer coefficient is changed similarly with flying velocity, but the extent is discrepant. Firstly, the heat-transfer coefficient decreases rapidly and then increases until reaching a maximum, after it slowly drops off, and the former two processes that have steep gradients are concentrated in the warhead area. For the cone-shaped part, the coefficient of convection heat transfer is proportional to the square root of the velocity in laminar conditions, while the ratio is 4/5 in the turbulent flow conditions. Accordingly, the coefficient of convection heat transfer reaches a maximum at the moment of launching, and then, it drops rapidly in the terminal trajectory. Apparently, the coefficient of convection heat transfer fluctuation increases by a

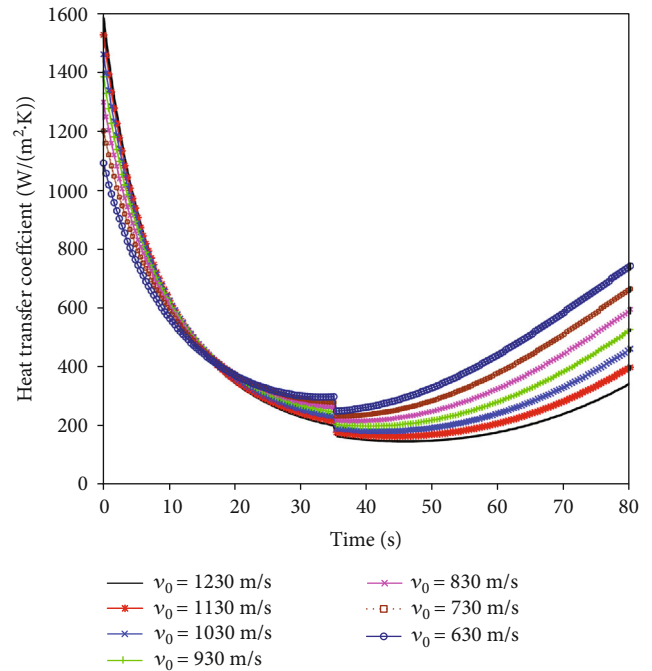


FIGURE 10: Average coefficients at different launch velocities.

small fraction in the midcourse of trajectory, which is responsible for the laminar-turbulent transition.

To get the effects of launch conditions on the coefficient of convection heat transfer, the influencing factors which include the launching velocity, spinning speed, and launching angle are analyzed, as shown in Figures 10–12. It can be found from the calculation results that the average heat-transfer coefficient increases with launching velocity in the first half of the trajectory, and the decrement grows rapidly at the same time. However, the coefficient is inversely proportional to the initial velocities during the second half of the trajectory, and the launching angle yields a similar tendency. Although the smaller launching angle will lead to more serious aerodynamic heating, it will not be reflected until the body has been launched for a short time. Furthermore, the effects of spinning speed are more noticeable at the high-speed stage, yet the effects will be weakened gradually with a reduction of velocity.

5. Conclusions

In this article, dynamic aerothermal characteristics on the surface of a cone-cylinder spinning flight body are reconstructed using updated modeling approaches, and the thermal node-network method is successfully applied for predicting the aerothermal environment of the body coupling motion of precession, spinning, and pitching. The exterior trajectory datum and the coefficient of convection heat transfer during the flight are synchronously obtained. The main results of this work are as follows:

- (1) The flight velocity is decreasing exponentially in the ascending period of the trajectory, and the

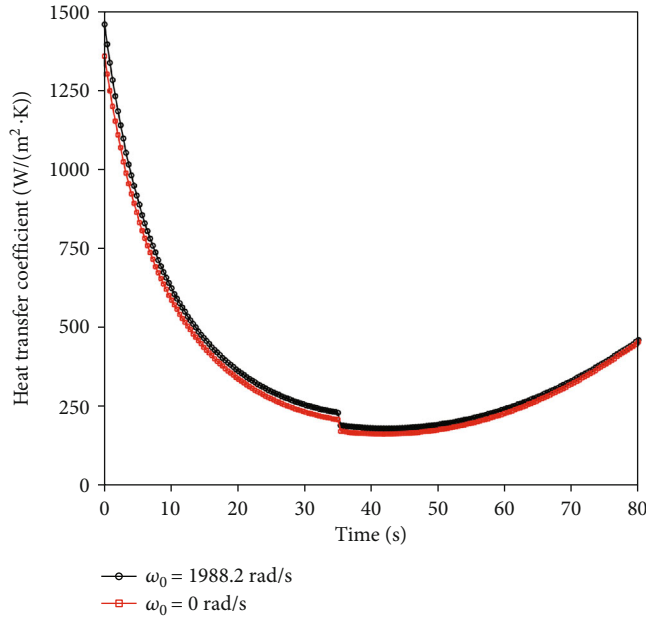


FIGURE 11: Average coefficients of convection heat transfer at different initial rotational speeds.

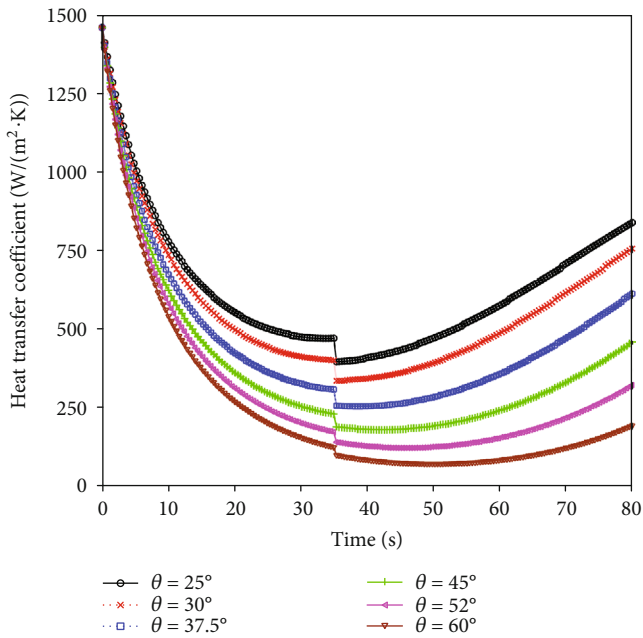


FIGURE 12: Average coefficients of convection heat transfer at different launch angles.

attenuation rates are quicker with the initial velocities. The exponential attenuation rate of angular speed in the ascending period is faster than in the descending. Besides, the average reference temperature on the surface of the conical part is significantly higher than that of the cylindrical part in the first 20 seconds of the trajectory, especially in a short time after launching. After 20 seconds, the average reference temperature on the conical surface is lower than that of the cylindrical part

- (2) The average coefficient of convection heat transfer is increasing with the initial velocity and rotational speed, and the attenuation rates are growing rapidly at the ascending stage during the flight, whereas the coefficient is inversely proportional to the initial velocity at the descending stage, and the shot angle is changed similarly. Additionally, the transient coefficient of convection heat transfer is dropping sharply at the beginning, and rising dramatically before a slow attenuation
- (3) Aerothermal characteristic is determined not only by the current flight state but also by the heat transfer environment during the flight, which is a progressive, lasting, and dynamic process. In consideration of the spinning speed, the coefficient of convection heat transfer is obviously too high to disregard, especially in supersonic regimes

Nomenclature

- d : Diameter, m
 m : Mass, kg
 t : Time, s
 Δs : Area of surface panel, m^2
 ρ : Density, kg/m^3
 cp : Specific heat capacity, $J/(kg \cdot K)$
 α : Cone-shaped angle, rad
 λ : Thermal conductivity, $W/(m \cdot K)$
 κ : Adiabatic index
 \mathbf{n} : Normal vector of surface panel
 A : Equatorial moment of inertia
 C : Polar moment of inertia
 \mathbf{v} : Velocity, m/s
 ω : Angular speed, rad/s

μ : Dynamic viscosity, (N·s)/m²
 η : Rifling angle, rad
 h : Heat transfer coefficient, W/(m²·K)
 δ_1 : Elevation attack angle, rad
 δ_2 : Azimuth attack angle, rad
 φ_1 : Elevation angle in the x direction, rad
 φ_2 : Azimuth angle in the x direction, rad
 ψ_1 : Elevation angle in the velocity direction
 ψ_2 : Azimuth angle in the velocity direction, rad
 T : Temperature, K
 P : Pressure, Pa
 H : Total enthalpy, J
 Nu : Nusselt number
 Re : Reynolds number
 Pr : Prandtl number.

Subscripts

w : Wall
 i : Compute node
 x : Axial direction
 r : Relative values
 ∞ : Freestream condition
 $*$: Flow parameter at reference temperature condition.

Data Availability

The [MATLAB calculation procedures] data used to support the findings of this study are available from the corresponding author upon request.

Conflicts of Interest

The authors declare that there is no conflict of interest regarding the publication of this paper.

Acknowledgments

This work was supported by the Natural Science Foundation of China (NSFC) under the Grant Number of 11372136, the Shanghai Municipal Science and Technology Commission of China (SMSTCC) under the Grant Number of 17050502000, and the Shanghai Ocean University under the Grant Number of A2-2006-20-200210.

References

- [1] T. Ozawa, T. Suzuki, and K. Fujita, "Aerodynamic measurements and computational analyses in hypersonic rarefied flows," *AIAA Journal*, vol. 53, no. 11, pp. 3327–3337, 2015.
- [2] C. J. Alban, A. N. Palazotto, and J. L. Rutledge, "Thermal considerations with respect to sliding contact at high speed," *Journal of Thermophysics and Heat Transfer*, vol. 30, no. 1, pp. 54–61, 2016.
- [3] M. B. Gerdroodbary, M. Imani, and D. D. Ganji, "Investigation of film cooling on nose cone by a forward facing array of micro-jets in hypersonic flow," *International Communications in Heat and Mass Transfer*, vol. 64, pp. 42–49, 2015.
- [4] S. Eyi, K. M. Hanquist, and I. D. Boyd, "Aerothermodynamic design optimization of hypersonic vehicles," *Journal of Thermophysics and Heat Transfer*, vol. 33, no. 2, pp. 392–406, 2019.
- [5] X. Pan, X. Wang, R. Wang, and L. Wang, "Infrared radiation and stealth characteristics prediction for supersonic aircraft with uncertainty," *Infrared Physics & Technology*, vol. 73, pp. 238–250, 2015.
- [6] S. P. Mahulikar, H. R. Sonawane, and G. Arvind Rao, "Infrared signature studies of aerospace vehicles," *Progress in Aerospace Sciences*, vol. 43, no. 7-8, pp. 218–245, 2007.
- [7] G. Bingtao, W. Xiaorui, C. Yujiao, L. Zhaohui, and Z. Jianlei, "High-accuracy infrared simulation model based on establishing the linear relationship between the outputs of different infrared imaging systems," *Infrared Physics & Technology*, vol. 69, pp. 155–163, 2015.
- [8] R. Savino, M. de Stefano Fumo, D. Paterna, and M. Serpico, "Studio aerodinamico di sistemi di protezione termica basati su UHTC," *Aerospace Science and Technology*, vol. 9, no. 2, pp. 151–160, 2005.
- [9] Y. Takahashi and K. Yamada, "Aerodynamic-heating analysis of sample-return capsule in future Trojan-asteroid exploration," *Journal of Thermophysics and Heat Transfer*, vol. 32, no. 3, pp. 547–559, 2018.
- [10] M. B. Gerdroodbary and S. M. Hosseinalipour, "Numerical simulation of hypersonic flow over highly blunted cones with spike," *Acta Astronautica*, vol. 67, no. 1-2, pp. 180–193, 2010.
- [11] M. B. Gerdroodbary, M. Imani, and D. D. Ganji, "Heat reduction using counterflowing jet for a nose cone with aerodisk in hypersonic flow," *Aerospace Science and Technology*, vol. 39, pp. 652–665, 2014.
- [12] S. Zhou, Z. O'Neill, and C. O'Neill, "A review of leakage detection methods for district heating networks," *Applied Thermal Engineering*, vol. 137, pp. 567–574, 2018.
- [13] J. Huang, P. Li, and W. Yao, "Thermal protection system gap analysis using a loosely coupled fluid- structural thermal numerical method," *Acta Astronautica*, vol. 146, pp. 368–377, 2018.
- [14] G. R. Inger, "Nonequilibrium boundary-layer effects on the aerodynamic heating of hypersonic waverider vehicles," *Journal of Thermophysics and Heat Transfer*, vol. 9, no. 4, pp. 595–604, 1995.
- [15] X. I. A. Yang, J. Urzay, S. Bose, and P. Moin, "Aerodynamic heating in wall-modeled large-Eddy simulation of high-speed flows," *AIAA Journal*, vol. 56, no. 2, pp. 731–742, 2018.
- [16] S. Zhang, F. Chen, and H. Liu, "Time-adaptive, loosely coupled strategy for conjugate heat transfer problems in hypersonic flows," *Journal of Thermophysics and Heat Transfer*, vol. 28, no. 4, pp. 635–646, 2014.
- [17] D. Knight, O. Chazot, J. Austin et al., "Assessment of predictive capabilities for aerodynamic heating in hypersonic flow," *Progress in Aerospace Sciences*, vol. 90, pp. 39–53, 2017.
- [18] D. Knight, J. Longo, D. Drikakis et al., "Assessment of CFD capability for prediction of hypersonic shock interactions," *Progress in Aerospace Sciences*, vol. 48-49, pp. 8–26, 2012.
- [19] D. Knight, H. Yan, A. G. Panaras, and A. Zheltovodov, "Advances in CFD prediction of shock wave turbulent boundary layer interactions," *Progress in Aerospace Sciences*, vol. 39, no. 2-3, pp. 121–184, 2003.
- [20] Y. Zheng and Z. Qiu, "Uncertainty propagation in aerodynamic forces and heating analysis for hypersonic vehicles with

- uncertain-but-bounded geometric parameters,” *Aerospace Science and Technology*, vol. 77, pp. 11–24, 2018.
- [21] M. Y. M. Ahmed and N. Qin, “Metamodels for aerothermodynamic design optimization of hypersonic spiked blunt bodies,” *Aerospace Science and Technology*, vol. 14, no. 5, pp. 364–376, 2010.
- [22] M. Y. M. Ahmed and N. Qin, “Recent advances in the aerothermodynamics of spiked hypersonic vehicles,” *Progress in Aerospace Sciences*, vol. 47, no. 6, pp. 425–449, 2011.
- [23] M. Y. M. Ahmed and N. Qin, “Numerical investigation of aeroheating characteristics of spiked blunt bodies at Mach six flight conditions,” *Aeronautical Journal*, vol. 115, no. 1168, pp. 377–386, 2011.
- [24] M. Y. M. Ahmed and N. Qin, “Surrogate-based multi-objective aerothermodynamic design optimization of hypersonic spiked bodies,” *AIAA Journal*, vol. 50, no. 4, pp. 797–810, 2012.
- [25] M. Y. M. Ahmed and N. Qin, “Investigation of flow asymmetry around axi-symmetric spiked blunt bodies in hypersonic speeds,” *Aeronautical Journal*, vol. 118, no. 1200, pp. 169–179, 2014.
- [26] Q. Qin, J. Xu, and S. Guo, “Fluid-thermal analysis of aerodynamic heating over spiked blunt body configurations,” *Acta Astronautica*, vol. 132, pp. 230–242, 2017.
- [27] M. B. Gerdroodbary, “Numerical analysis on cooling performance of counterflowing jet over aerodisk blunt body,” *Shock Waves*, vol. 24, no. 5, pp. 537–543, 2014.
- [28] M. B. Gerdroodbary, S. Bishehsari, S. M. Hosseinalipour, and K. Sedighi, “Transient analysis of counterflowing jet over highly blunt cone in hypersonic flow,” *Acta Astronautica*, vol. 73, pp. 38–48, 2012.
- [29] L. Wang, Y. Li, Z. Zhao, and Z. Liu, “Transient thermal and pressurization performance of LO2 tank during helium pressurization combined with outside aerodynamic heating,” *International Journal of Heat and Mass Transfer*, vol. 62, pp. 263–271, 2013.
- [30] M. G. Persova, Y. G. Soloveichik, V. K. Belov et al., “Modeling of aerodynamic heat flux and thermoelastic behavior of nose caps of hypersonic vehicles,” *Acta Astronautica*, vol. 136, pp. 312–331, 2017.
- [31] T. G. Vincent, E. N. Rolfe, K. T. Lowe, and J. A. Schetz, “Aerodynamic analysis of total temperature probe thermal performance using conjugate heat transfer,” *Journal of Thermophysics and Heat Transfer*, vol. 33, no. 3, pp. 830–843, 2019.
- [32] P. Duda, “A method for transient thermal load estimation and its application to identification of aerodynamic heating on atmospheric reentry capsule,” *Aerospace Science and Technology*, vol. 51, pp. 26–33, 2016.
- [33] N. Li, Z. Lv, S. Wang, G. Gong, and L. Ren, “A real-time infrared radiation imaging simulation method of aircraft skin with aerodynamic heating effect,” *Infrared Physics & Technology*, vol. 71, pp. 533–541, 2015.
- [34] S. I. Siltou, “Navier-Stokes computation's for a spinning projectile from subsonic to supersonic speeds,” *Journal of Spacecraft and Rockets*, vol. 42, no. 2, pp. 223–231, 2005.
- [35] D. S. James, *CFD prediction of Magnus effect in subsonic to supersonic flight*, U.S. Army Research Laboratory, ARL-TR-4929, 2009.